JOURNAL OF GEOPHYSICAL RESEARCH, VOL. 113, B08308, doi:10.1029/2007JB005468, 2008

Click Here for Full Article

Influence of near-surface volcanic structure on long-period seismic signals and on moment tensor inversions: Simulated examples from Mount Etna

Christopher Bean,[1] Ivan Lokmer,[1] and Gareth O'Brien[1]

Received 27 October 2007; revised 21 April 2008; accepted 15 May 2008; published 7 August 2008.

[1] Long-period (LP) seismicity on volcanoes is thought to be associated with moving fluids or resonating fluid-filled conduits, hence LP moment tensor (MT) source inversions might have a direct bearing on our understanding of the plumbing system. Using 3-D full wavefield simulations and 2-D sensitivity kernels in a digital elevation model of Mount Etna, we investigate the influence of near-surface volcanic structure on LP signals and on moment tensor inversions. Contrary to common wisdom in crustal seismology we find that, despite their relatively long wavelengths, LPs are severely distorted by near-surface structures including layering and topographic features. In particular near-surface low-velocity structures which are commonly observed on volcanoes play a critical role in controlling the nature of LP signals. If not accounted for, these path effects leak into the source solution, leading to the emergence of erroneous source geometries, spurious forces and incorrect source time functions. This is particularly problematic if one adopts an ''unconstrained'' solution space for the source, with many free parameters. Hence there is a fine balance in the trade-off between the velocity model and the source. In the absence of high-resolution near-surface velocity control we demonstrate the importance of employing a priori source information from other fields (e.g., structural geology), for shallow LPs, constraining the number of free parameters in the inversion. A probabilistic approach should then be taken, as the model with the ''best fit'' is not necessarily the ''true'' solution.

Citation: Bean, C., I. Lokmer, and G. O'Brien (2008), Influence of near-surface volcanic structure on long-period seismic signals and on moment tensor inversions: Simulated examples from Mount Etna, *J. Geophys. Res.*, *113*, B08308, doi:10.1029/2007JB005468.

1. Introduction

[2] Volcanoes can exhibit a wide variety of seismic signal types. These variations are a consequence of complex volcanic environments which can include rock fracturing, gas and liquid movement, rough topography, a heterogeneous edifice, possible strong site effects and the intertwining of different wave types, in the near field. Understanding the relationships between this variability and the consequent seismic signals is important when assessing the temporal evolution of volcanic activity. Long-period (LP) events with dominant periods in the range 0.2–2 Hz have received particular attention as they are thought to be associated with moving fluids or resonating fluid-filled conduits [e.g., *Chouet*, 1996; *Neuberg et al.*, 2000]. Understanding when and how fluids move in a volcanic environment is of paramount importance. Increases in the occurrence rate of LP events often herald a new episode of unrest. Inverting for LP source mechanisms is becoming increasingly common in an effort to better understand fluid-driven processes [*Kumagai et al.*, 2005, 2002a; *Legrand et al.*, 2000; *Nakano et al.*, 2003]. LP events often occur at shallow depths (e.g., 0–800 m [*Saccorotti et al.*, 2007], approximately 200 m [*Kumagai et al.*, 2002a], 200–400 m [*Nakano et al.*, 2003], 200–600 m [*Almendros et al.*, 2001]) and therefore have short path lengths. They also have kilometer-long wavelengths hence the role of edifice heterogeneity has been assumed to be negligible and has largely been ignored (although it has recently been recognized that surface topography can distort their signals [*Cesca et al.*, 2008; *Kumagai et al.*, 2005; *Neuberg and Pointer*, 2000]).

[3] A striking feature of the morphology of volcanic edifices is the layered nature of the near-surface stratigraphy. Strong lithologically controlled seismic impedance contrasts can occur at layer interfaces depending on eruptive history, and can be compounded by near-surface fracturing. Laboratory measurements on rock samples from the Trecase borehole close to Mount Vesuvius [*Bruno et al.*, 1998] show that the mean unfractured *P* wave velocity in the top 300 m is less than 2.5 km s^{-1}. An abrupt transition occurs at about 300 m, leading to a mean value of about 3.5 km s^{-1} in the depth range 300–1500 m. Surface wave dispersion analyses reveal similar results for Vesuvius [*De Luca et al.*, 1997], Stromboli [*Chouet et al.*, 1998], Puu Oo Hawaii [*Ferrazzini et al.*, 1991], Arenal, Costa Rica [*Mora et al.*, 2006] and

[1]Seismology and Computational Rock Physics Laboratory, School of Geological Sciences, University College Dublin, Belfield, Dublin, Ireland.

Copyright 2008 by the American Geophysical Union.
0148-0227/08/2007JB005468$09.00

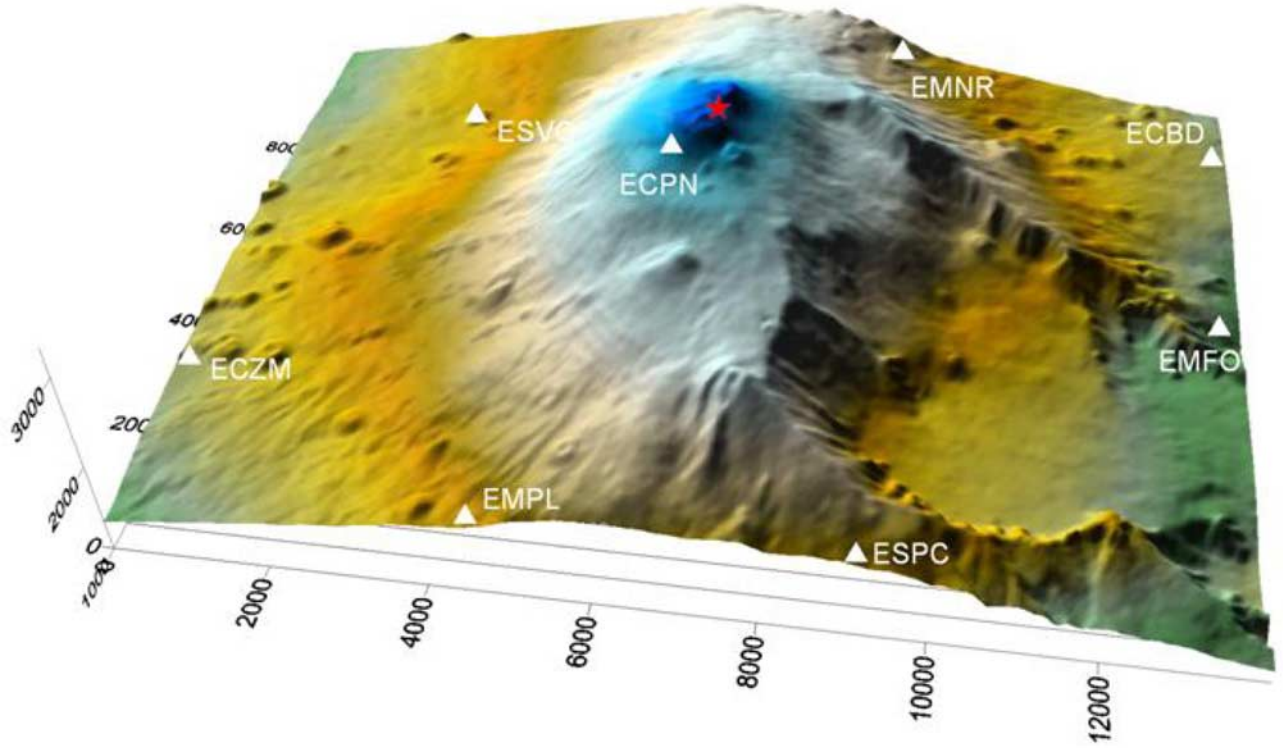

Figure 1. Mount Etna topography and broadband seismic network. The star denotes both the epicenter of the shallow LP activity occurring over the past few years and the epicentral position of the synthetic source used in our simulations. Axes units are in meters.

Masaya, Nicaragua [*Métaxian et al.*, 1997], with mean *P* wave velocities in the top 300 m of $\sim$ 2.0 km s^{-1}. In all cases the mean *P* wave velocities are less than 1 km s^{-1} in the top 80 m. Using array analysis of tremor wavefields, *Saccorotti et al.* [2003] also determined low-velocity shallow structures at Kilauea. Importantly they find significant discrepancies between tomographically derived velocities [*Dawson et al.*, 1999] and *Saccorotti et al.*'s [2003] tremor derived results. The tomography model at Kilauea overestimates shallow (<500 m) velocities, by up to 1 km s^{-1} for *S* waves, and does not properly represent the shallow structure. *Saccorotti et al.* [2003] attribute this discrepancy to a lack of very shallow earthquakes in the tomographic inversion, a point likely to be relevant to the majority of velocity models derived for volcanoes. Although less pronounced, similar discrepancies can be seen at Mount Etna by comparing near-surface (<350 m) velocities from array-derived surface wave dispersion studies [*Saccorotti et al.*, 2004] with high-resolution tomographic images [*Patanè et al.*, 2006]. Hence it seems that near-surface (few hundred meters) low velocities are common in volcanic environments. Here we investigate the effects of near-surface structure on the waveforms of LP events and we consider the implications for LP source inversions, using simulated examples from Mount Etna.

2. Models and Data

[4] Our approach is to use 3-D full wavefield numerical simulations [*O'Brien and Bean*, 2004a] to calculate synthetic seismograms in media both with and without superficial low-velocity layers. In previous work, simulations including homogeneous half-spaces [*Kumagai et al.*, 2002a; *Legrand et al.*, 2000; *Nakano et al.*, 2003], homogeneous velocity models with topography to investigate wavefield effects [*Ripperger et al.*, 2003] and for Green's functions calculations [*Kumagai et al.*, 2005] have been considered. Here we add near-surface edifice velocity structure and in addition include topography, employing a digital elevation model (DEM) of Mount Etna, with a 40 m horizontal grid step (Figure 1). Our synthetic recording station positions mirror the actual locations of permanent broadband field stations on Mount Etna (Figure 1). We use synthetic LP seismograms computed at these station positions in our simulation to invert for synthetic source mechanisms using a moment tensor (MT) inversion procedure, the results of which are compared with our known input sources. Sensitivity kernels are calculated to help with the interpretation of some of the wave propagation effects seen in the simulations.

[5] Seismograms are generated in (1) a homogenous model, Vp = 3500 m s^{-1}, Vs = 2000 m s^{-1}, and (2) the same model as in (1), replacing the top 400 m with a single low-velocity layer, Vp = 2000 m s^{-1}, Vs = 1200 m s^{-1}. To save on computational expense, these low velocities are slightly higher than measured values in the top 400 m on Mount Etna, estimated using surface wave dispersion analysis [*Saccorotti et al.*, 2004], and hence will lead to an underestimation of any calculated wave distortions. All densities are derived from relationships given by *Corsaro and Pompilio* [2004].

[6] We use a point source with a mechanism equivalent to that of a vertical tensile crack, with the crack-normal

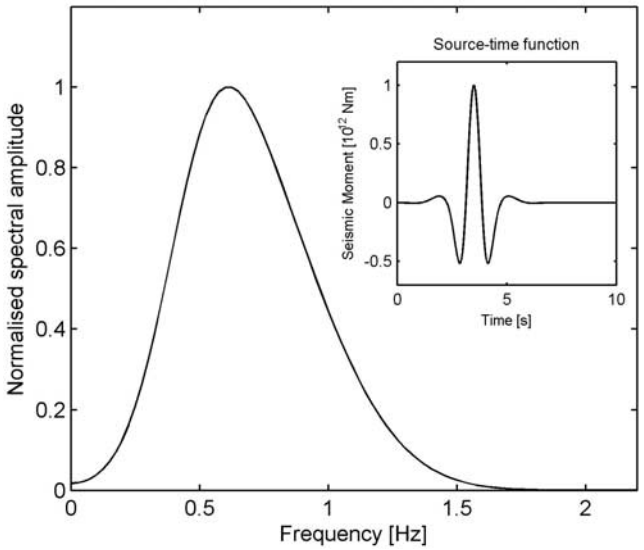

Figure 2. Amplitude spectrum of source used in the simulations and (inset) the source time function.

oriented in an E-W direction (see next section). The source time function is a (modified) Ricker wavelet with a dominant frequency of 0.7 Hz (Figure 2). The details of the input source time function are not important in this study; what is important is an assessment of our ability to recover the input source parameters by inverting our synthetic seismograms. We consider three individual cases in which the source is at different depths, all located beneath the epicenter of actual LP activity on Mount Etna (see Figure 1). The model space is 28.2 × 25.6 × 9.9 km, including absorbing boundaries to suppress edge reflections of 2.8, 2.8 and 5 km, in the x, y and z directions respectively. The DEM topography acts as a free surface. Three component synthetic seismograms for stations ECPN, ECZM, EMFO, EMPL for source depths, 120, 600 and 1800 m below the maximum surface height (summit, elevation approximately 3320 m asl) are shown in Figures 3, 4 and 5 respectively. Top and bottom traces denote the seismograms calculated for the homogeneous and layered models, respectively. The ratios between the maximum peak-to-peak amplitudes for synthetic seismograms recorded at the same stations in the two models are given in the upper right corner of each plot.

[7] Figures 3, 4 and 5 demonstrate that the near-surface low-velocity layer has a significant influence on the recorded traces. Both the wave amplitudes and the signal durations are modified by the layer. The primary focus of this paper is to quantify the consequences of waveform distortion, due to the layer, on our ability to recover the source mechanism. We the exception of the ''test'' section of this paper, in the following only data from the layered model are employed in source inversions.

3. Moment Tensor Source Inversions

3.1. Description of the Method

[8] We apply frequency domain moment tensor (MT) inversion to our synthetic seismograms. As volcanic LP sources are thought to involve mass transport (gas and/or liquid) a single-force term is usually added to the standard equations used for the inversion [e.g., *Kumagai et al.*, 2005; *Nakano et al.*, 2003], yielding:

$$u_n^s(\omega) = G^s_{np,q}(\omega) \cdot M_{pq}(\omega) + G^s_{np}(\omega) \cdot F_p(\omega), \quad n,p,q = x,y,z, \tag{1}$$

where u_n^s is the nth component of displacement at the station s, and $G^s_{np,q}$ and G^s_{np} are the Green's functions, i.e., the nth component of the response of the medium at the station s to the force couples M_{pq} and single forces F_p, respectively, applied at the source. The inversion is performed for each frequency and solutions for M_{pq} and F_p are then transformed to the time domain. If we form the column vector **d** that contains all the data components for all the stations, the matrix **G** containing the Green's functions and column vector **m** containing the moment tensor and single-force components, equation (1) can be rewritten in the form:

$$\mathbf{d} = \mathbf{Gm}, \tag{2}$$

[9] Equation (2) is solved for **m** by minimizing the squared error [*Menke*, 1984]. The waveform misfit is defined by the residual function, R, as follows:

$$R = \frac{(\mathbf{d} - \mathbf{Gm})^T(\mathbf{d} - \mathbf{Gm})}{\mathbf{d}^T\mathbf{d}} \tag{3}$$

[10] Three inversions are performed on simulated data for each of three source depths, resulting in nine separate inversions. The input data to the inversion procedure are from the layered model (Figures 3 (bottom), 4 (bottom) and 5 (bottom)). The inversions are as follows: (1) inversion for the 6 independent moment tensor components and 3 single forces (this is becoming common practice when inverting for volcano sources [e.g., *Kumagai et al.*, 2005; *Nakano et al.*, 2007] for LPs, [*Chouet et al.*, 2003; *Ohminato et al.*, 1998] for very long period (VLP) sources), (2) inversion for the moment tensor only, and (3) inversion for a constrained model of a crack. The crack orientation is treated as an unknown and is sought by searching for the crack orientation for which the residual function is minimum. Hence we make three ''guesses'' at a possible source model with different degrees of freedom: the first two do not take account of the a priori source information actually used in the simulations; the third exploits some of this information, the fact that it is a crack, although the known crack orientation is not used to aid the inversion. This mimics a typical real-world situation, where we often have no a priori information or sometimes have limited information from other evidence (e.g., geological/structural).

[11] Knowledge of the Green's functions is needed in order to carry out the inversion procedure (see equation (2)). Using our wave simulator, synthetic Green's functions are calculated for a homogeneous velocity model, without near-surface low-velocity layers but including DEM topography for Mount Etna. We take this approach because, for real data inversions, near surface velocity structure (1) is often not known and (2) to date is not included in the inversion

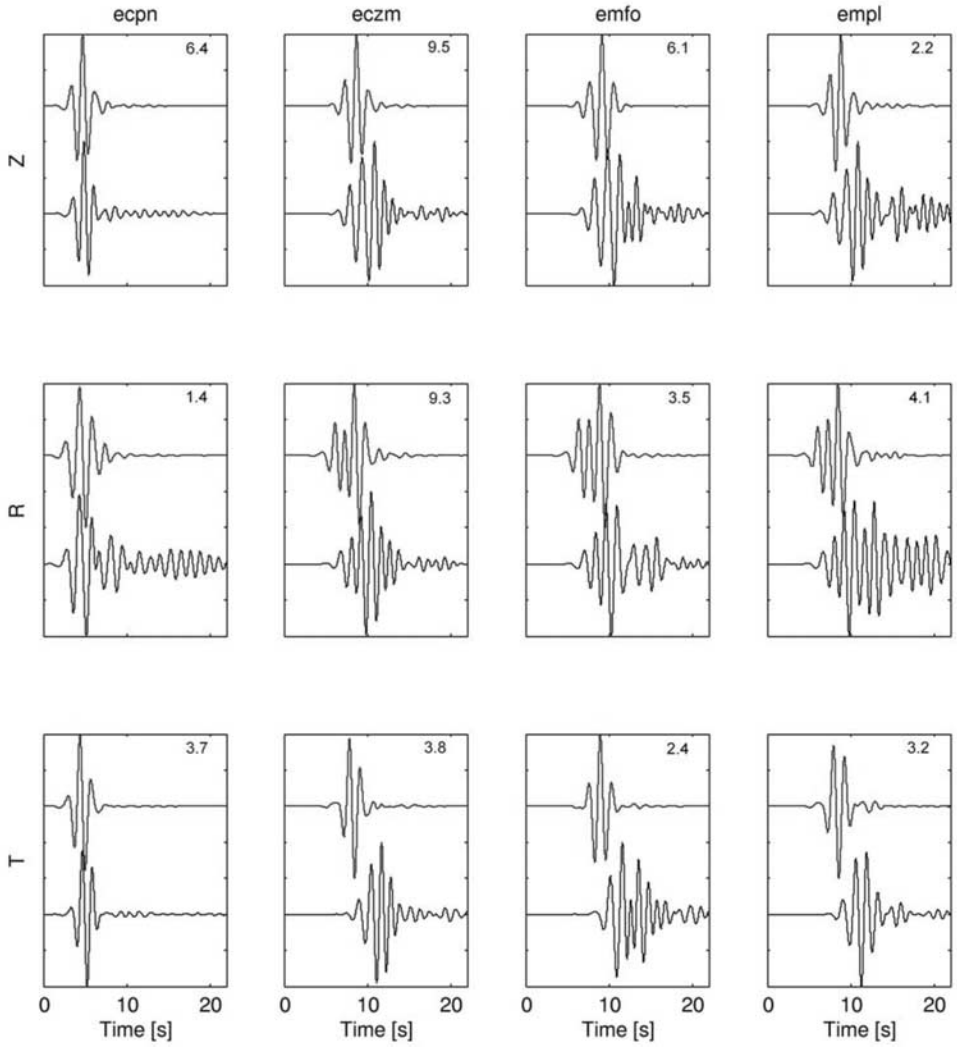

Figure 3. Synthetic seismograms calculated for two velocity models, for the source depth 120 m below the surface. The epicentral location and station positions are marked in Figure 1. Source mechanism is equivalent to that of a vertical crack with the crack normal oriented in the E-W direction. For a given station and component, the top traces in each panel denote the signals calculated for the homogeneous model with *P* and *S* wave velocities 3500 and 2000 m s^{-1}, respectively. The bottom traces in each panel are seismograms calculated for the model with the 400 m thick superficial low-velocity layer. All traces are individually normalized. Ratios (layered/homogeneous) of the peak-to-peak amplitudes are given in the top right corner of each panel. Amplifications in the layered model are evident.

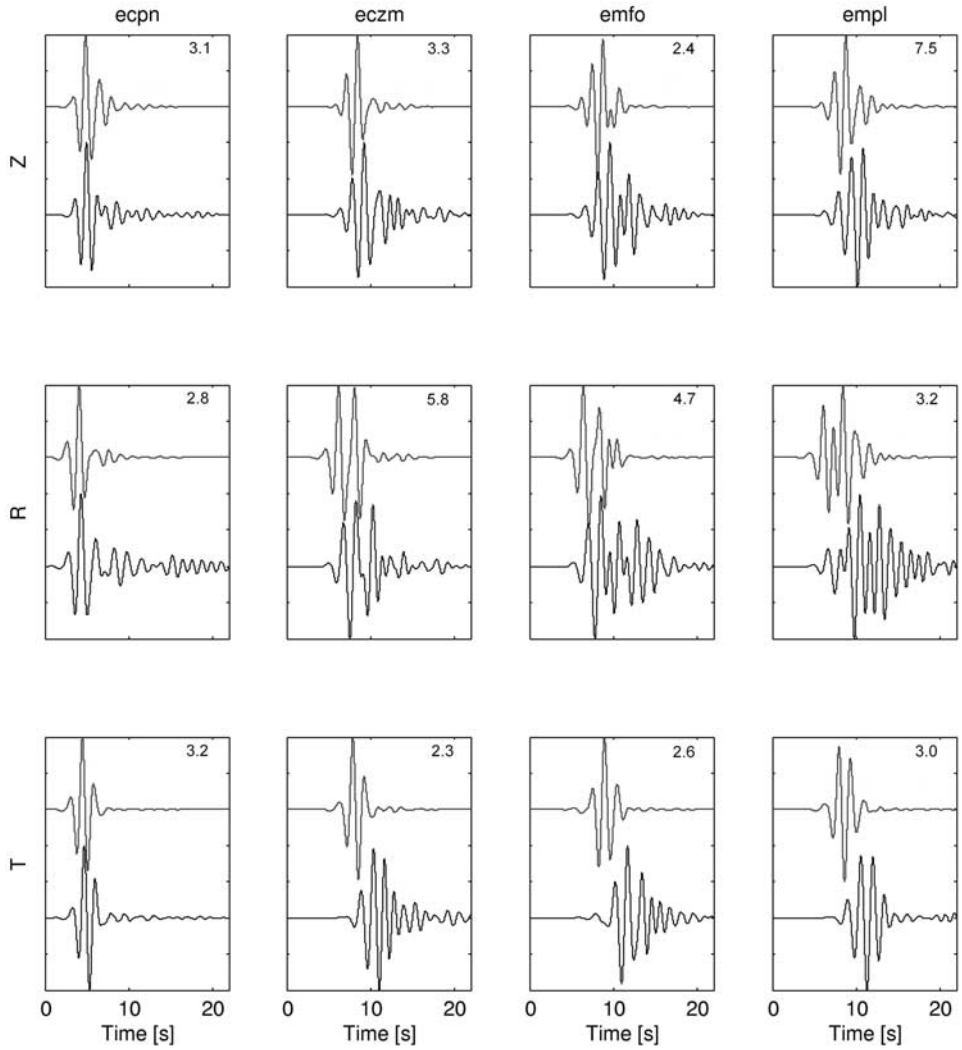

Figure 4. Same as Figure 3, except source is at a depth of 600 m.

procedure. Once we have built the Green's function library without low-velocity layers, we then simulate our LP events using the source described in the next section, in velocity models with low-velocity layers. Our aim here is to replicate the realistic situation where the uppermost part of the velocity structure is poorly resolved and consequently the low-velocity layers are not used when calculating the Green's functions. We take this approach as low-velocity layers which are not accounted for often exist on real volcanoes, as outline above. We have more than the minimum 25 model-grid points per minimum seismic wavelength representing the free surface in the low-velocity layer, as needed in some numerical schemes [e.g., *Ohminato and Chouet*, 1997].

3.2. Description of the Input Source in the Simulations

[12] The seismograms in Figures 3, 4 and 5 were generated using a point source with a mechanism equivalent to that of a vertical tensile crack, with the crack-normal oriented in the x direction (E-W). The source time function is a (modified) Ricker wavelet with the dominant frequency of 0.7 Hz. Our model has a Poisson's ratio of 0.25. Cartesian moment tensor components for the tensile crack can be expressed in a spherical coordinate system by the following set of equations [*Nakano and Kumagai*, 2005]

$$\begin{aligned} M_{xx} &= M_0\left({}^{\lambda}\!/_{\mu} + 2\sin^2\theta\cos^2\varphi\right),\\ M_{yy} &= M_0\left({}^{\lambda}\!/_{\mu} + 2\sin^2\theta\sin^2\varphi\right),\\ M_{zz} &= M_0\left({}^{\lambda}\!/_{\mu} + 2\cos^2\theta\right),\\ M_{xy} &= M_0\sin^2\theta\sin 2\varphi,\\ M_{xz} &= M_0\sin 2\theta\cos\varphi,\\ M_{yz} &= M_0\sin 2\theta\sin\varphi, \end{aligned} \tag{4}$$

where angles θ and ϕ are defined as shown in Figure 6, and $M_0 = \mu dV$, where dV is the incremental volume change. λ and μ are Lamé's constants.

[13] For a vertical crack with crack-normal oriented in the x direction ($\theta = 90°$, $\phi = 0°$), equations (4) reduce to:

$$M = M_0 \cdot \begin{bmatrix} \frac{\lambda}{\mu}+2 & 0 & 0 \\ 0 & \frac{\lambda}{\mu} & 0 \\ 0 & 0 & \frac{\lambda}{\mu} \end{bmatrix} \rightarrow \text{ for } \lambda = \mu \rightarrow M_0 \cdot \begin{bmatrix} 3 & 0 & 0 \\ 0 & 1 & 0 \\ 0 & 0 & 1 \end{bmatrix} \tag{5}$$

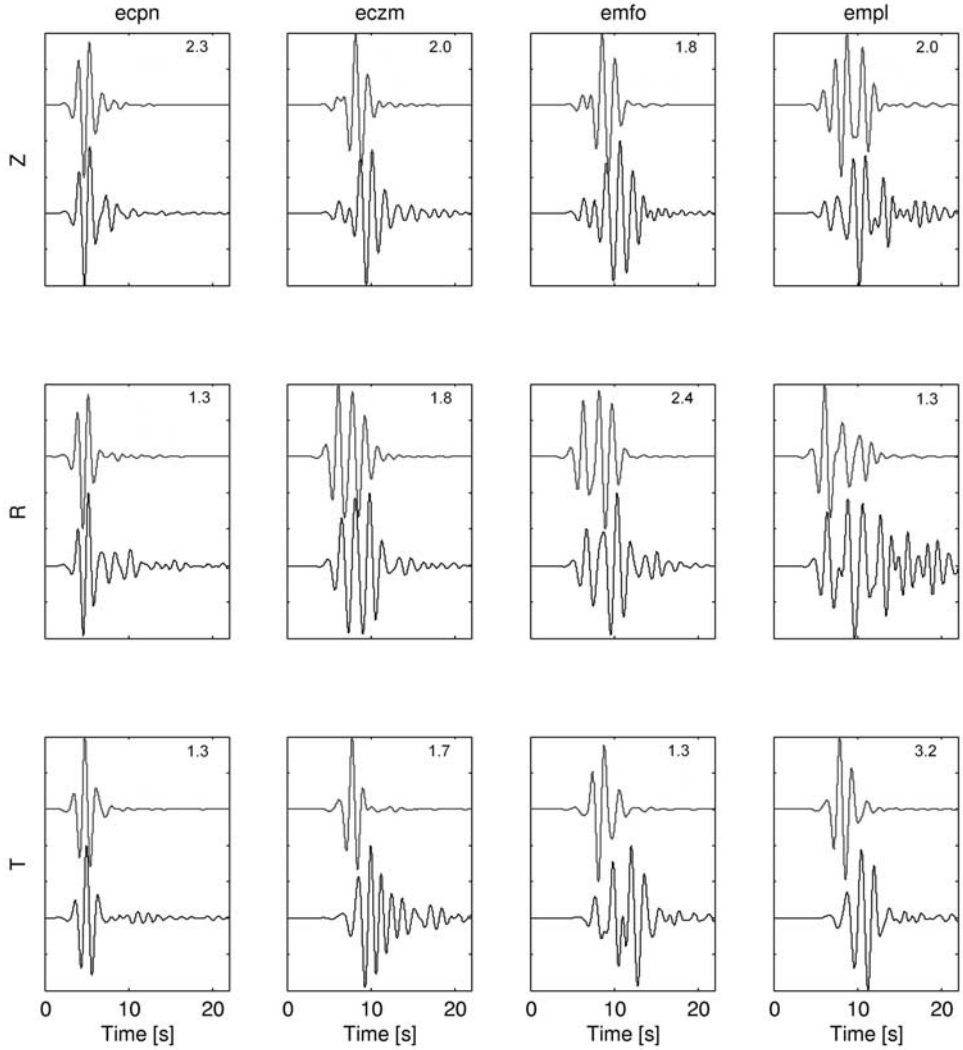

Figure 5. Same as Figure 3, except source is at a depth of 1800 m.

[14] Equation (5) describes the input sources used in the simulations, where the source time evolution is given in Figure 2.

3.3. Testing the Simulation and Inversion Method

[15] Our method has two principal steps: (1) inputting sources according to equation (5) into a 3-D forward modeling full wavefield simulator and (2) applying MT inversions (which use our synthetic Green's function library, calculated in a homogeneous model including Etna topography) on synthetic seismograms calculated in inhomogeneous (layered) models using the simulator, in an attempt to recover information about the source. Before we can say anything meaningful about the consequences of our ignorance of near-surface structure on LP source inversion, we start by demonstrating that our method yields reliable results. For the test we construct a new Green's function library (as described above) in a velocity model which includes the 400 m thick near-surface low-velocity layer and Etna DEM topography, thus accurately taking into account the response of the medium for which LP point

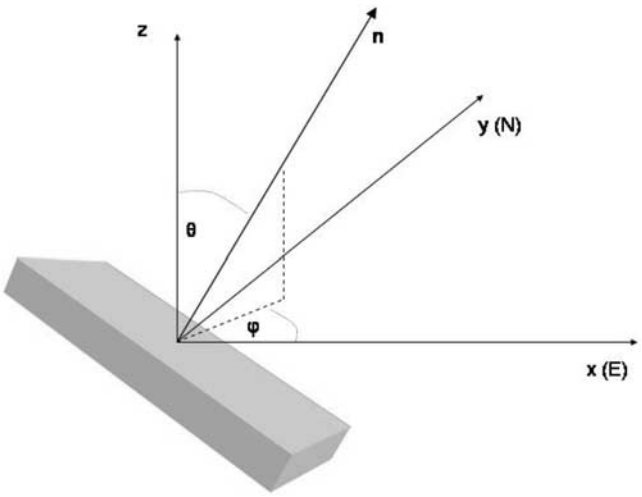

Figure 6. Crack orientation in a spherical coordinate system.

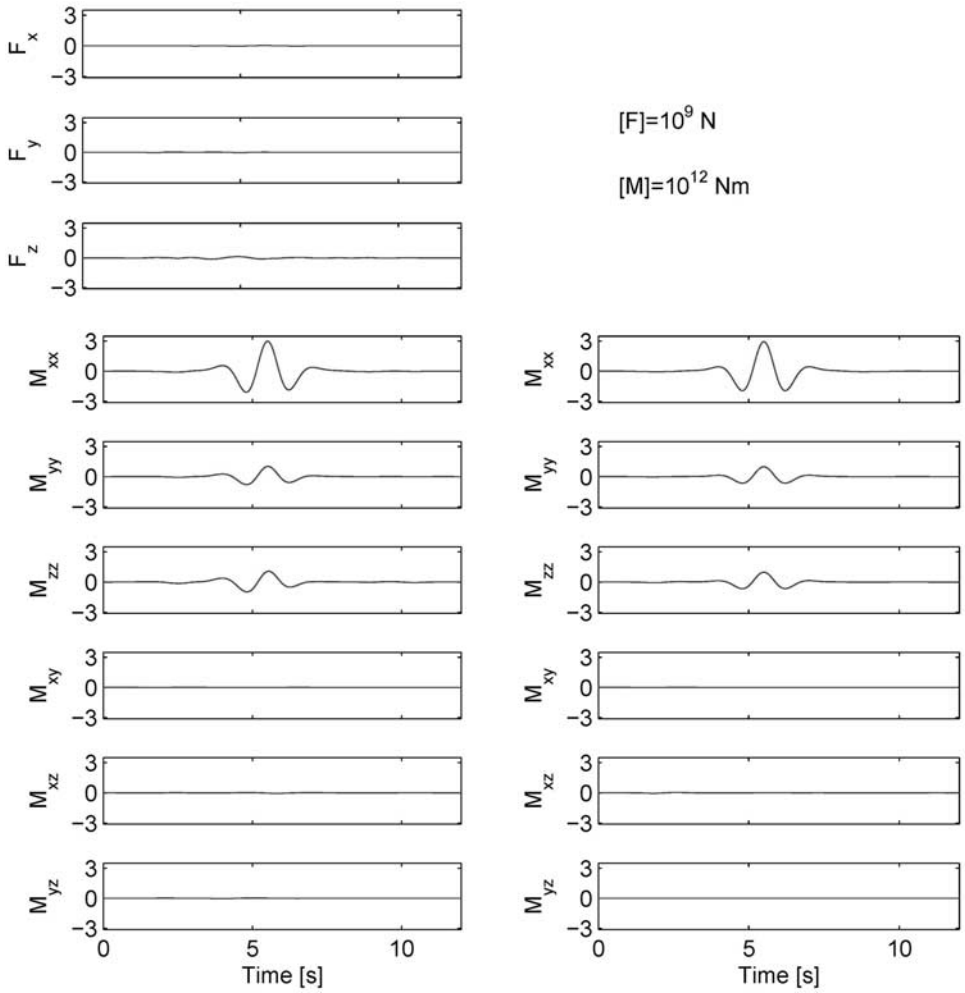

Figure 7. Test of the inversion and simulation procedures. (left) The solution from the inversion for the moment tensor and single-force components. (right) The solution from the inversion for the moment tensor only. The source depth was 120 m, and the synthetics and the Green's functions were both calculated in the layered model. In both cases the source time function as well as the source mechanism was successfully recovered. Residual in both cases was R = 0.003.

sources are simulated. MT inversion (equations (2) and (3)) is performed on the resulting seismograms, for a 120 m deep source with the epicentral position of real LPs recorded at the positions of the actual seismic stations on Etna (Figure 1).

[16] For the inversion we allow all components to be unconstrained, including single forces. Following the inversion we apply the method of *Vasco* [1989] to determine if all components can be represented by a common function. If such a function exists, we can infer a source mechanism from its coefficients for different MT components.

[17] Comparing Figure 7 with Figure 2 and considering equation (5), the results demonstrate that we can successfully recover the known source parameters. Even in the case where we allow for a possible single force component in the solution, no such force is found, consistent with our input source. The relative amplitudes of the MT components approximately match equation (5) and the time-history (Figure 2) is also successfully recovered.

3.4. Effects of Low-Velocity Layers on Recovery of Accurate Source Parameters

[18] It is clear that the near-surface low-velocity layer has an appreciable effect on the seismograms in Figures 3, 4 and 5. MT inversions are carried out on the seismograms from the layered model, to quantify the significance of that effect on our ability to determine source parameters. The Green's function library used for these inversions is determined for a homogeneous model, with topography. Three source depths and three possible source models are considered.

3.5. MT Only and MT With Single Force; Source Depth: 120 m

[19] It can be seen in Figure 8 that the "MT only" solution is unstable, yielding what appears to be a temporal change of the source mechanism (see Figure 7 for a graphical representation of the "correct" solution) and this solution would likely be rejected on the basis of a blind inversion, where no a priori information about the source is

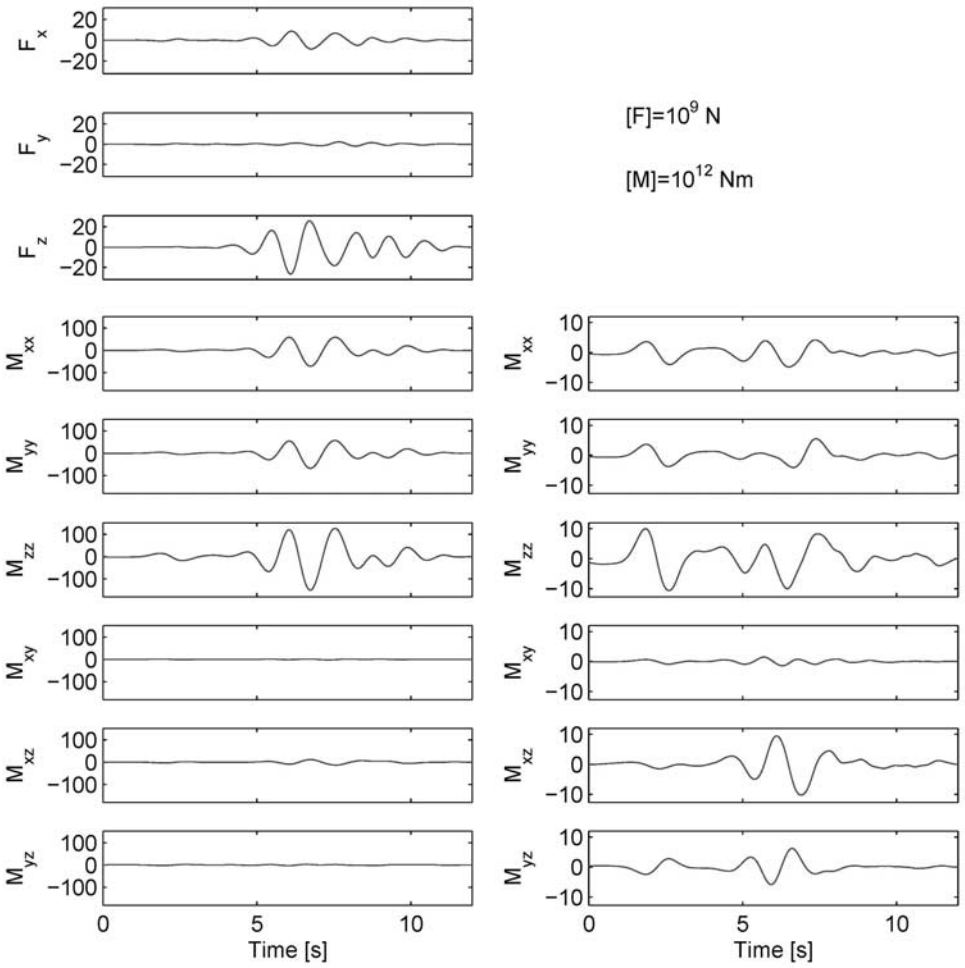

Figure 8. Moment tensor solution for the 120 m deep source. (left) The solution for the moment tensor and single-force components. (right) The solution from the inversion for the moment tensor only. The synthetics and the Green's functions were calculated using layered and homogeneous models, respectively.

known. However, the ''MT with single force'' solution looks stable and realistic. We suggest that this solution would likely be accepted in a blind inversion (see Table 1 for misfit statistics). Comparing the solution with Figures 2 and 7 and with equation (5) demonstrates that it is clearly incorrect and misleading. In fact the solution suggests the presence of a horizontal crack with MT components 1:1:2 and the presence of a spurious vertical force contributing about 20% to the signal. Furthermore the source time function has opposite sign and a magnitude 50 times larger than the input source.

3.6. MT Only and MT With Single Force; Source Depth: 600 m

[20] As in the case of the shallower source, the solution for a source at 600 m is also problematic (Figure 9). Both solutions (MT only and MT with single force) give similar source mechanisms, but both are incorrect. The MT only is suggestive of a crack whose normal is inclined at about 30° from its true value, possessing a strong double couple component. The MT with single force implies a crack whose normal is inclined at approximately 40° to its true value and a strong spurious single force is also apparent in the direction of the crack normal.

3.7. MT Only and MT With Single Force; Source Depth: 1800 m

[21] The solution for a source at 1800 m is a better approximation to the input source than the shallower cases (Figure 10). It should be noted that in this case all seismic stations are either at the same level as or above the seismic sources. Both MT only and MT with single force give similar mechanisms and their magnitudes are in the right order relative to the input source. Importantly however, despite the better fit for the deeper source (located 1400 m below the bottom of the low-velocity layer), the MT with single force solution still produces a spurious single force, contributing about 50% to the signal.

3.8. MT Solution for a Tensile Crack; Source Depths: 120, 600 and 1800 m

[22] Thus far we have not placed any a priori constraint on the possible geometrical structure of the source. However, in some instances either previous studies or geological

Table 1. Inversion Parameters for the Three Source Depths and Three Inversion Models[a]

	MT + SF	MT	CRACK
	H = 120 m		
Moment tensor eigenvalues	1:1:2.3	unstable	1:1:3
Inclination of the main axis of MT solution from the crack normal (deg)	83.1	-	10.0
Ratio(SF/MT)	0.27E-3	-	-
Misfit	0.2434	0.4324	0.8081
AIC	−19096	−9746	−3736
	H = 600 m		
Moment tensor eigenvalues	1:1.3:2.3	1:3:4	1:1:3
Inclination of the main axis of MT solution from the crack normal (deg)	39.1	34.0	5.0
Ratio(SF/MT)	0.66E-3	-	-
Misfit	0.2943	0.5891	0.7664
AIC	−13627	−840	−5262
	H = 1800 m		
Moment tensor eigenvalues	1:3.4:8.6	1:1.4:3.2	1:1:3
Inclination of the main axis of MT solution from the crack normal (deg)	1.0	4.0	0.0
Ratio(SF/MT)	0.47E-3	-	-
Misfit	0.2283	0.3487	0.6437
AIC	−20940	−15942	−10287

[a]Read, e.g., 0.27E-3 as 0.27×10^{-3}. MT, moment tensor; SF, single force; CRACK, inversion solutions which were constrained, a priori, to have a crack geometry; H, depth; AIC, Akaike information criterion.

or other observations will limit the possible range of likely geometries. Here we constrain the solution to the "geologically likely" situation of a tensile crack. Crack azimuth (ϕ) and dip ($90 - \theta$) (Figure 6) are arbitrary and are determined as part of the solution.

[23] The best solutions for all three source depths in terms of θ, ϕ and the source time function are given in Figure 11. All three solutions are close to the actual input source, in terms of azimuth, dip and time-history. Consistent with the results above, the deepest source yields a marginally better fit.

[24] In order to help quantify some of the underlying causes for poor source parameter recovery outlined above, we need to track the space-time evolution of the wavefield.

3.9. Estimating the Sensitivity of the Wavefield to Model Parameters: Sensitivity Kernels

[25] It is clear that the introduction of the shallow low-velocity layer has a major impact on the wavefield. In this section we look at the underlying reasons for that impact, using 2-D full wavefield simulations and sensitivity kernels. We ask the question: What part of the velocity model is the wavefield sensitive to, for any given time window in our seismogram? Using ideas from seismic inversion [*Tarantola*, 1984, 1987, 1988] time reversal mirrors [*Fink*, 1997] and adjoint methods [*Talagrand and Courtier*, 1987]; *Tromp et al.* [2005] give an integrated theoretical framework for the calculation of such sensitivities. In this work we implement the expressions given by *Tromp et al.* [2005]. Two numerical simulations in the velocity model are required: (1) a "regular" simulation, where a source is input and a synthetic seismogram is calculated at the recording station of interest, and (2) an "adjoint" simulation where the part of the seismogram under investigation (i.e., the time window of interest from the seismogram) is extracted, time reversed and used as an input source (the adjoint source). The adjoint source is located at the receiver location from the first simulation, and recorded at the location which was occupied by the source in the first (regular) simulation. Individual sensitivity kernels for *P* and/or for *S* waves can then be calculated by looking at the interaction between the regular and adjoint wavefields [e.g., *Tromp et al.*, 2005]. We calculate *P* and *S* wave 2-D kernels for both ECPN and ECZM stations, in both a homogeneous and a layered (400 m thick near surface low-velocity layer) model, for source depths of 120 m and 1800 m. All simulations include topography, taken as a 2-D cut of the 3-D DEM, through stations ECPN, ECZM and the summit. The source time function for the regular simulation is the same as in the 3-D simulations, Figure 2. *P* wave (*S* wave) sensitivity kernels are calculated by integrating the product of the divergence (curl) of the regular and adjoint wavefields, over the time interval of interest. Figure 12 shows the seismograms for the regular simulation. As was seen in the 3-D simulations, the near surface low-velocity layer significantly distorts the wavefield, particularly for ECZM station, located on the flank. *P* wave and *S* wave sensitivity kernels for station ECZM for the shallow source are shown in Figures 13 and 14 respectively. These sensitivity kernels indicate the area of the velocity model that contributes to the wavefield which is arriving at the station, within the seismogram time slice under investigation. The "polarity" of the sensitivity is related to the polarity of the field divergence (*P* waves) or curl (*S* waves). For our purpose, the magnitude of the sensitivity is the most important parameter. It is important to note that these sensitivity plots are not analogous to regular wave propagation snapshots, but are more instructive as they map seismogram arrivals precisely onto model properties, and tell us which areas of the model are "sampled" by the wavefield for specific times in the seismic wave train, recorded at a specified station. For finite frequencies the wavefield can "see beyond" the station, even in a homogeneous model (e.g., Figure 14, second row on the left, 7–10 s). This effect will be more pronounced for longer-period data. The sensitivity kernels allow us to better quantify the underlying causes of the extended wave trains seen in Figure 12, for the layered model. Comparing Figures 13 and 14 it is clear that most of the seismogram is composed of *S*-type wave motion. Figure 12 also demonstrates that vertical and horizontal components are approximately 90° out of phase, indication the presence of Rayleigh waves. Even for long-wavelength (LP) events one might intuitively expect that waves will be trapped in the low-velocity layer; what is not so obvious in advance is the importance of this phenomenon and the extensive "footprint" of the sensitivity. For example, Figure 14, first row on the right, 0–7 s demonstrates that the first 0–7 s of the wavefield arriving from the summit to a flank station is primarily controlled by the combined effects of near-summit velocity and topographic structure. Perhaps surprisingly for a source located close to the summit, the structure on the opposing flank, on the side facing away from the station, also makes a significant contribution to the signal arriving at ECZM, located approximately 6 km from the summit. In seismology, "reverberations" are often attributed to site effect,

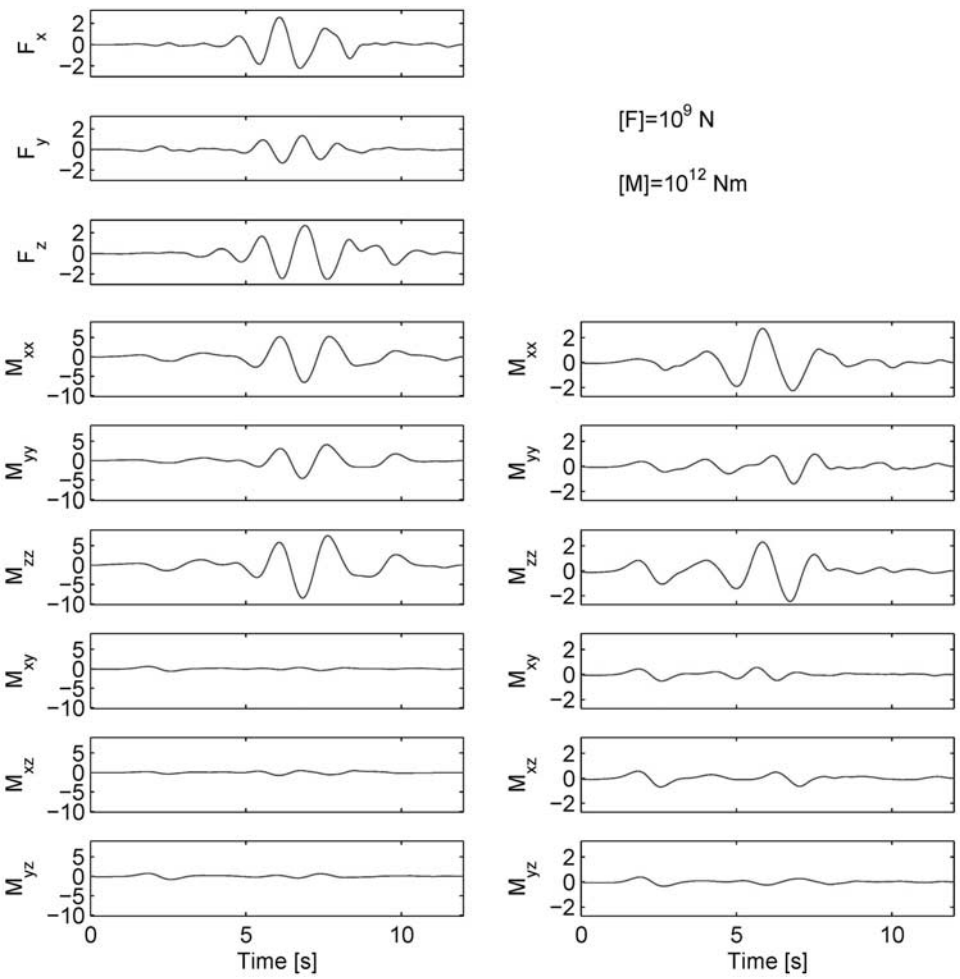

Figure 9. Same as Figure 8 except moment tensor solution for a 600 m deep source.

which is clearly not the case in this example. Although the signals for the layered model in Figure 12 looks reverberatory, the underlying cause is not local to the station. Comparing the left and right sides of the second row in Figures 13 and 14, it becomes clear that what appear to be stations related reverberations in Figure 12 are in fact trapped waves sampling large regions of the near-surface edifice. This point is even more visible in Figure 15 for summit station ECPN. For the 10–15 s time slice (Figure 15, third row on the right) the seismogram comprises contributions from across the surface of the entire edifice of Mount Etna. This is also true for *P* waves in the case of ECPN (Figure 16) which are much more prevalent for the summit station, relative to the flank station, further indicating the complexity and spatial variability of the wavefield. Even without resorting to kernel analysis, it can be seen from Figure 12 that the flank station recording is severely distorted by the near surface effects. In the above examples, the seismic source lies within the low-velocity layer, which will be the case for "shallow" LP events. Though less commonly recorded, deep LPs are likely to lie below layers with such low velocities. Figure 17 shows *S* wave kernels for ECZM station, for a source at 1800 m depth, 1400 m below the base of the low-velocity layer. Although the effects are not as pronounced as in the case of the shallower source, relative to the contribution made by the entire edifice the near surface layer still makes a disproportionate contribution to the wavefield arriving at the station.

4. Discussion

[26] The results of the inversions are summarized in Table 1. If a model is validated (by an assessment of the misfit) on the same data set from which it was estimated, the fit always improves as the flexibility of the model structures increases. The AIC information criterion [*Akaike*, 1974] can be used to test the significance of the number of free parameters. This criterion, often used to decide which MT solution best fits a data set [*Chouet et al.*, 2003; *Kumagai et al.*, 2005; *Nakano et al.*, 2003; *Ohminato et al.*, 1998], is included in Table 1. The criterion is based on the maximum likelihood approach for solving the inverse problem and enables us to estimate the expected decrease of the residual function with an increase in the number of model parameters. However, this assumes that we have a good knowledge of the medium through which the waves propagate. This condition is not always satisfied. In our case as we are inverting in the presence of an "unknown" near-surface low-velocity layer,

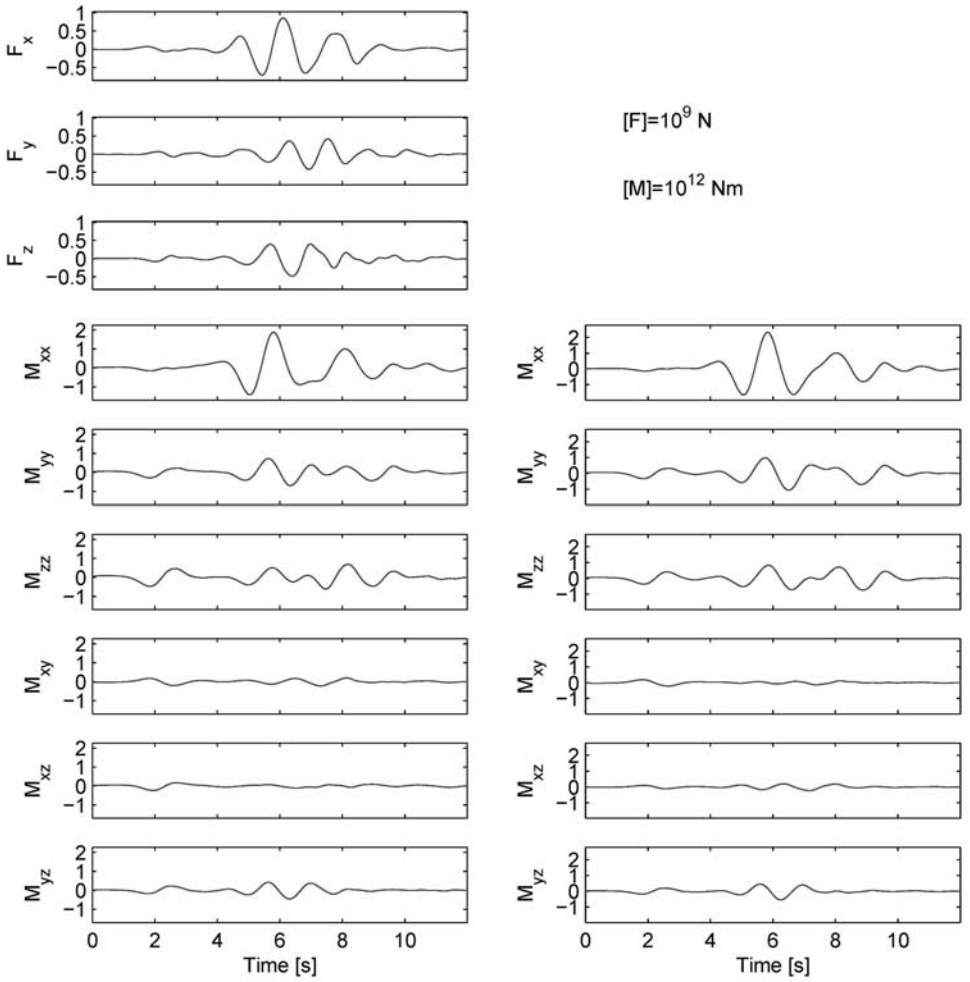

Figure 10. Same as Figure 8 except moment tensor solution for an 1800 m deep source.

so caution must be exercised when interpreting the AIC measure. This point is evident in the case of the 120 m deep source. The MT with single force inversion gives the best waveform fit and the smallest AIC number. The inversion looks very stable, but the solution is wrong in almost every respect (Figure 8): (1) horizontal instead of a vertical crack, (2) incorrect source time function, (3) wrong moment magnitude by a factor of 50, and (4) the existence of a spurious vertical force accounting for 20% of the signal. Although we might expect this outcome for the case where the seismic source is initiated in the low-velocity layer and the layer thickness is approximately $\lambda_s/4$, similar behavior is also observed for deeper sources, which lie below the bottom of the low-velocity layer. Of particular concern is the consistent appearance of a spurious single force whenever it is permitted in the inversion procedure. This would likely lead to the false interpretation of fluid injection/expulsion, the orientation of which is determined by the force vector. Another area of concern is the false oscillatory nature of the source–time function and the variations in the orientation of the MT eigenvectors (Figures 8, 9 and 10). When the Green's functions are calculated using the correct velocity model, the MT component magnitudes obtained are approximately correct, 3:1:1 (see Figure 7). When the velocity model is incorrect there is significant departure from these values, which can lead to incorrect measures of moment magnitudes and can mask information about the source radiation pattern, from which the mechanism is obtained.

[27] Two-dimensional sensitivity kernel calculations illustrate many of the underlying causes of the observations outline above. In short, even for low-frequency LP-type events, low-velocity layers of realistic physical dimensions as measured on volcanoes can ''trap'' waves leading to longer wave trains and distorted amplitudes. Rough topography complicates this picture. What should be noted is the size of the footprint for later arrivals in the seismograms, as demonstrated by the sensitivity kernels, often comprising contributions from across the surface of the entire shallow part of the edifice (e.g., Figure 15, third row on the right).

[28] LP signals play an important role in determining the physical and perhaps chemical state of a volcano, as they are thought to be a consequence of disturbances initiated by liquid/gas movement. Two aspects of particular importance are (1) what is the geometry of the structure(s) controlling mass migration and (2) what types of fluids are involved. MT inversion can help constrain the geometry. An accurate knowledge of the source time function is important in

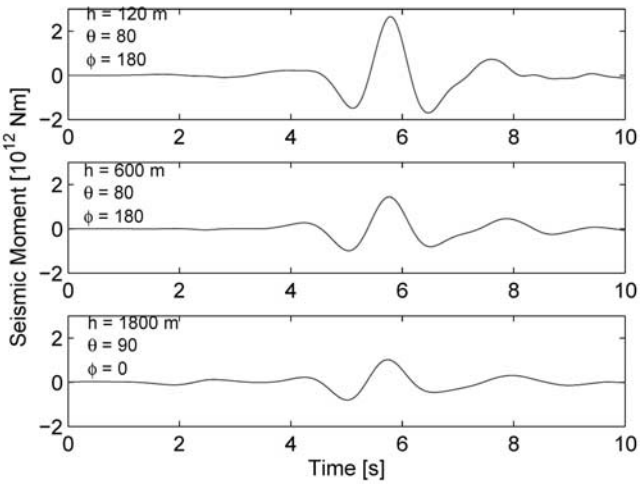

Figure 11. Moment tensor solutions for a tensile crack for the source depths 120, 600 and 1800 m. The orientation of the crack was obtained by performing a search in the (θ, φ) space with a step of 10°. Although the misfit function has a considerably higher value than for the inversions presented in Figures 8, 9 and 10 (see Table 1), all 3 solutions presented here are close to the true solution (the deepest source gives a slightly better solution). The crack orientation as well as the source time function is successfully recovered.

addressing (2), where source Q modeling can help limit the possible range of fluid types [e.g., *Kumagai and Chouet*, 1999; *Kumagai et al.*, 2002b; *Lokmer et al.*, 2008]. However, our simulation data demonstrate that, despite the long wavelengths associated with LP events, a 400 m thick low-velocity superficial layer can significantly distort the source signal. Such layers seem commonplace in volcanic settings. If care is not exercised in the inversion procedure, this distortion will preclude accurate estimates of (1) and (2). Although the effect is stronger for shallower sources, it is still pronounced even if the source lies outside/below the low-velocity layer.

[29] For comparison with our findings, by analyzing field seismograms *Harrington and Brodsky* [2007] demonstrate that shallow hybrid earthquakes at Mount St. Helens can be explained in terms of brittle failure coupled with a very complicated path and low rupture velocities. They reject the hypothesis of direct fluid involvement in source generation. We suggest that path effects can also play a significant role in controlling the recorded nature of LP events, particularly for stations located on the flanks of the volcano.

5. Conclusions

[30] We have demonstrated that simple near-surface velocity structure can have a detrimental effect on source inversions for LP seismic events. We use 3-D full wavefield numerical simulations, a realistic volcano-seismic source mechanism near-surface velocity structure and topography from Mount Etna and sensitivity kernel analysis. When the effects on the waveforms of these near-surface structures are not taken into account, they can lead to: (1) excessively long-source time functions, (2) spurious single forces, (3) misorientated source-cracks/conduits, and (4) incorrect estimates of moment magnitudes. The effect is particularly pronounced for, but not unique to shallow sources. If not properly accounted for these effects could preclude accurate estimates of the geometry of conduits controlling mass migration and of the nature of the fluids involved. As most volcanoes likely have very low-velocity near-surface layers, these distortions are probably ubiquitous. This observation contravenes well established assumptions in Earthquake seismology where long wavelengths are taken to be insensitive to smaller-scale heterogeneity/layering and consequently Green's functions can be calculated in homogeneous half-spaces. In contrast, on volcanoes the impedance contrasts at the near surface, the extreme topography and the geometric configuration of the seismic network, where shallow LP events can lie above the recording stations, all imply that the near surface structure cannot be ignored. Hence Green's functions should be calculated in a full 3-D space using full waveform simulations, despite their significant computational expense. Furthermore an important consideration when deploying networks for source inversions is to populate the summit area with as many stations as is feasible. For shallow LPs this observations is consistent with that of *Neuberg and Pointer* [2000], who suggest that broadband stations should be deployed as close to the source as possible.

[31] We have focused on the geological structural influences on source inversion results, however the sources themselves can of course be variable in nature. These considerations leave us with a philosophical dilemma as to how to approach this inverse problem, as outlined by *Tarantola* [2006]. Given that observations cannot be used to verify models but only to falsify them (no amount of observational fits prove the model, one misfit falsifies it) how much, if any, a priori information should be used? If for example no a priori near surface structural information is used then the solution in Figure 8 cannot falsify the apparent existence of a single force in the input source model. Regrettably, without such a "near-surface correction," an apparent single force might reappear in a variety of environments at different volcanoes, building a "body of evidence" for its existence. However, in our simulated data we can falsify it in two ways: (1) is trivial; we know that it doesn't exist because we have a priori information about the source. However, this will not help us in the real world, as we cannot access that information in advance and (2) we do not see any evidence for it in Figure 7 because (1) we have sufficient a priori information about the geological structure (exact knowledge in our case) and (2) our forward problem, our simulated data, has a unique solution (unlike the inverse problem). That is, given our sufficient knowledge of the geological structure we use the unique solution from our forward modeling procedure to falsify the existence of the single force. This is an extremely powerful outcome as it allows us to reject a hypothesis and consequently make some progress in our understanding of the source process (by knowing what it is not). The lesson here is that we must use as much a priori structural information as possible if we are to limit the solution space for the source, even to deriving new near surface structural models in advance of source inversions, if they are not already available.

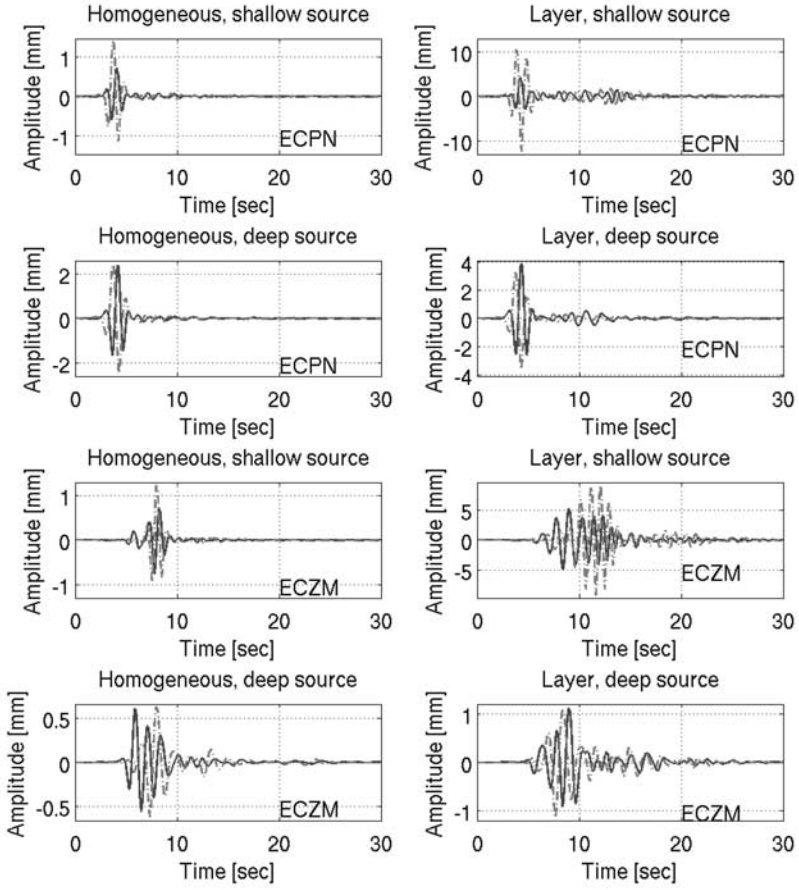

Figure 12. Synthetic seismograms for the regular 2-D simulation used for the construction of sensitivity kernels. ECPN and ECZM are station locations, as given in Figure 1. (left) Homogeneous and (right) layered models are shown. Shallow (120 m) and deep (1800 m) source depths are also indicated. Heavy solid: vertical component; Light dashed: horizontal (radial) component (positive corresponds to up and away from the source).

[32] Now that we have ''removed'' the structural component to the best of our ability, we are left to tackle the source itself: should we use a priori source information? There are many different source models which have been proposed for volcanoes [e.g., *Chouet*, 1986; *Julian*, 1994; *Neuberg et al.*, 2006; *O'Brien and Bean*, 2004b]. None of these models can be verified, merely falsified. For a given investigation the models which cannot be falsified within some acceptable fit to data are taken as solutions to the inverse problem. Drawing on work by *Tarantola* [2006], we suggest the following way forward: Undertake inversions for a range of structural models, based on the best a priori structural information available, using simulations to ''strip away'' structural effects, as presented herein. If the structural velocity model is known to be well constrained, it then allows for the exploration of a wider range of possible free parameters and hence a greater number of potential source models. If the structural velocity model is poorly constrained then near surface path effects which were not accounted for in the Green's function calculations leak into the source solution, increasing the size of the solution space for the source and leading to the emergence of artifacts. In this case the use of a priori source information becomes crucial and a solution should be sought by searching in a smaller parameter space, for a range of constrained source models. Constraints from structural geology, deformation, complementary geophysical or geochemical studies can be employed.

[33] Models which produce synthetic seismograms which give an ''unacceptable fit'' to the recorded field seismograms, according to some predefined criterion, are rejected. The population of models with an ''acceptable fit'' is a solution to the inverse problem. Naturally if all the a priori information is false then it reduces the probability of obtaining a fit, and these models are more likely, in a probabilistic sense, to be rejected. Importantly the converse applies for valid a priori information.

[34] Care must be taken not to adopt the best fit as the ''best model.'' In the examples presented in this paper, the MT with single force inversions give the best waveform fits (smallest misfits) and the smallest ''goodness of fit'' AIC numbers (Table 1); however the solution is completely wrong. Our a priori information constrained crack model gives the ''correct solution,'' but its goodness of fit is not as impressive.

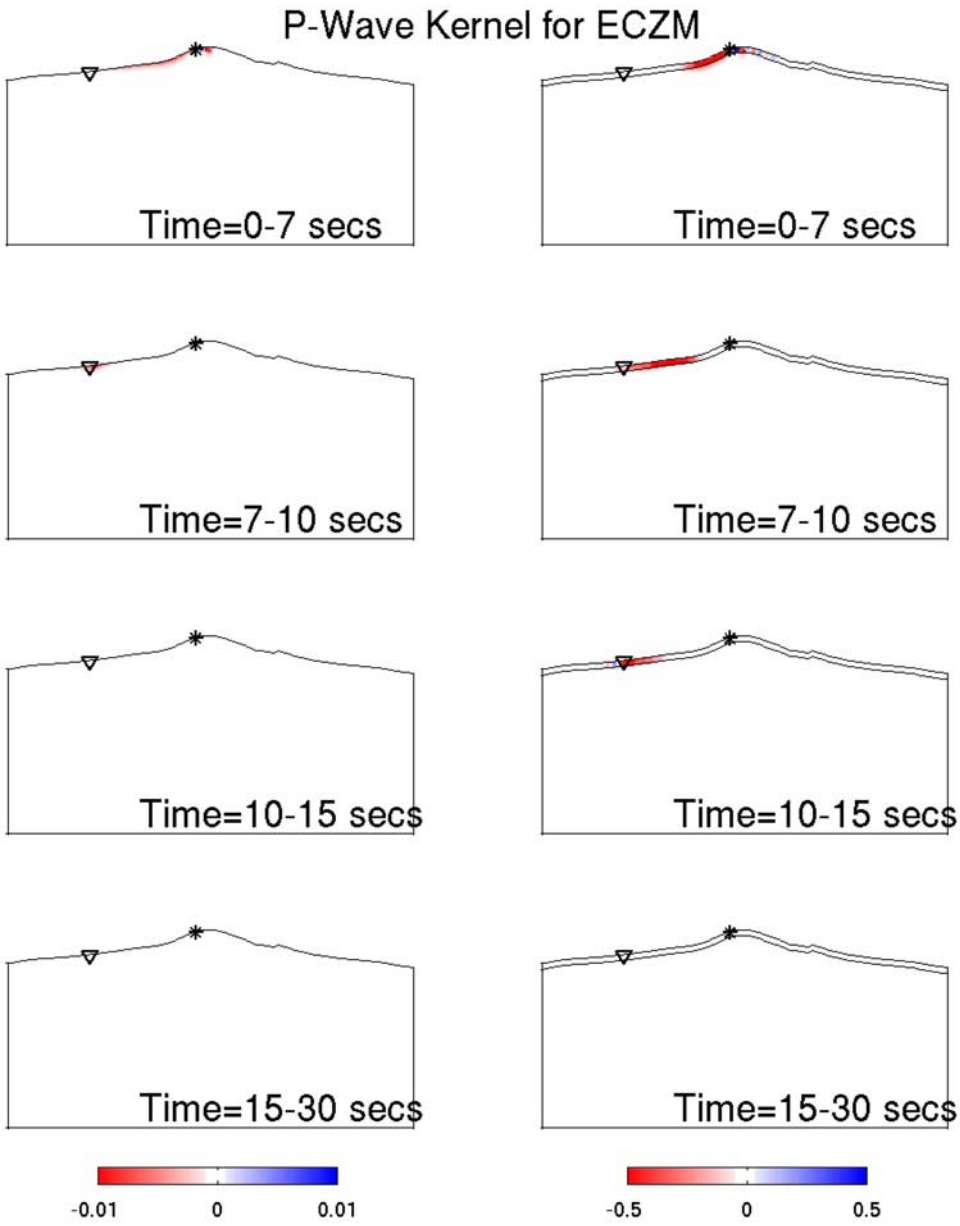

Figure 13. *P* wave sensitivity kernels for station ECZM (inverted triangle), for the (left) homogeneous and (right) layered models. The rows represent the different seismogram time slices for which the kernels are calculated, as indicated on Figure 13. Units are Kg m^{-1} s^{-1}. Source (star) depth, 120 m. Model is 20 km $\times$ 10 km. All kernels for a given model and source-station pair are relatively normalized.

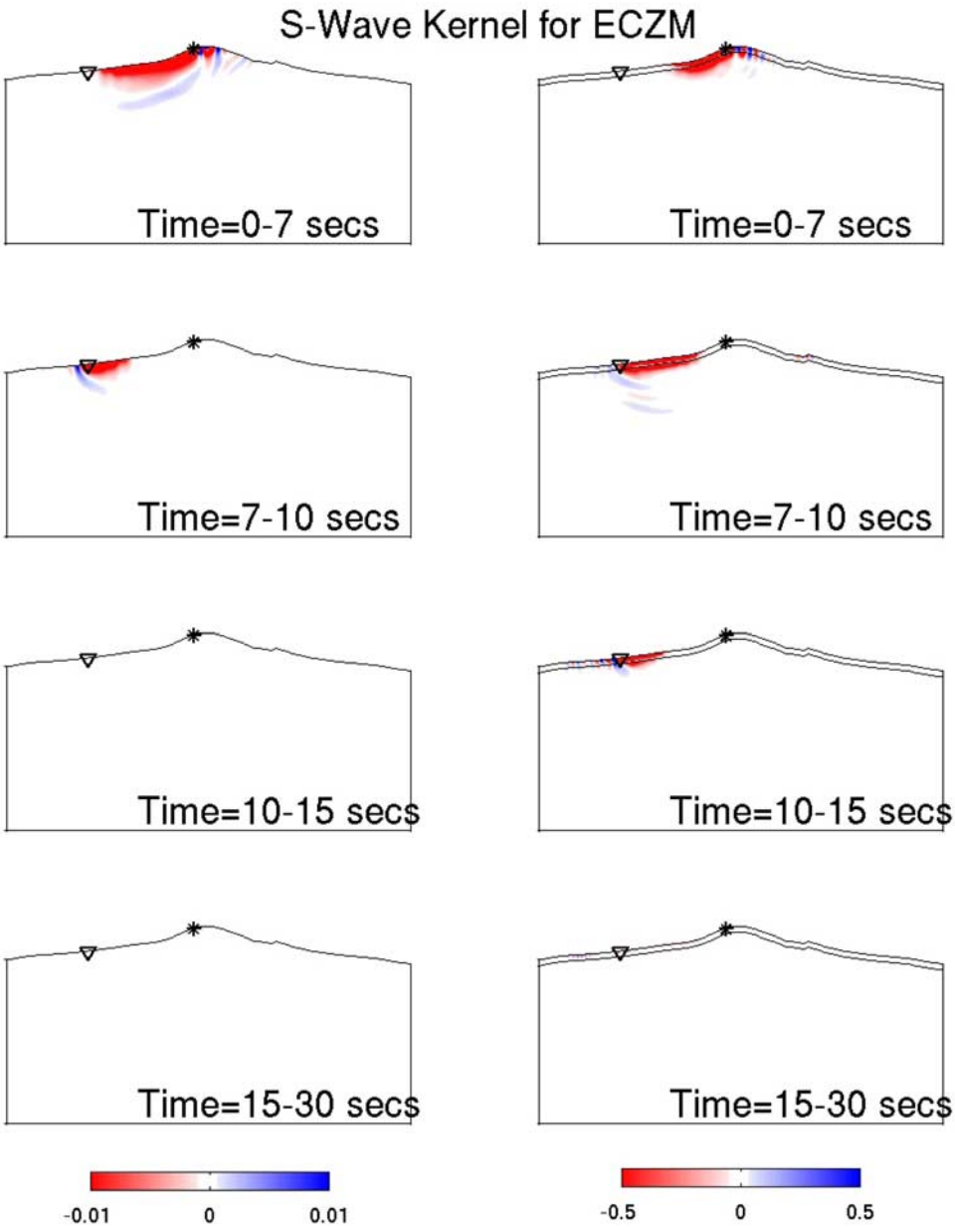

Figure 14. *S* wave sensitivity kernels for station ECZM, for the (left) homogeneous and (right) layered models. See Figure 13.

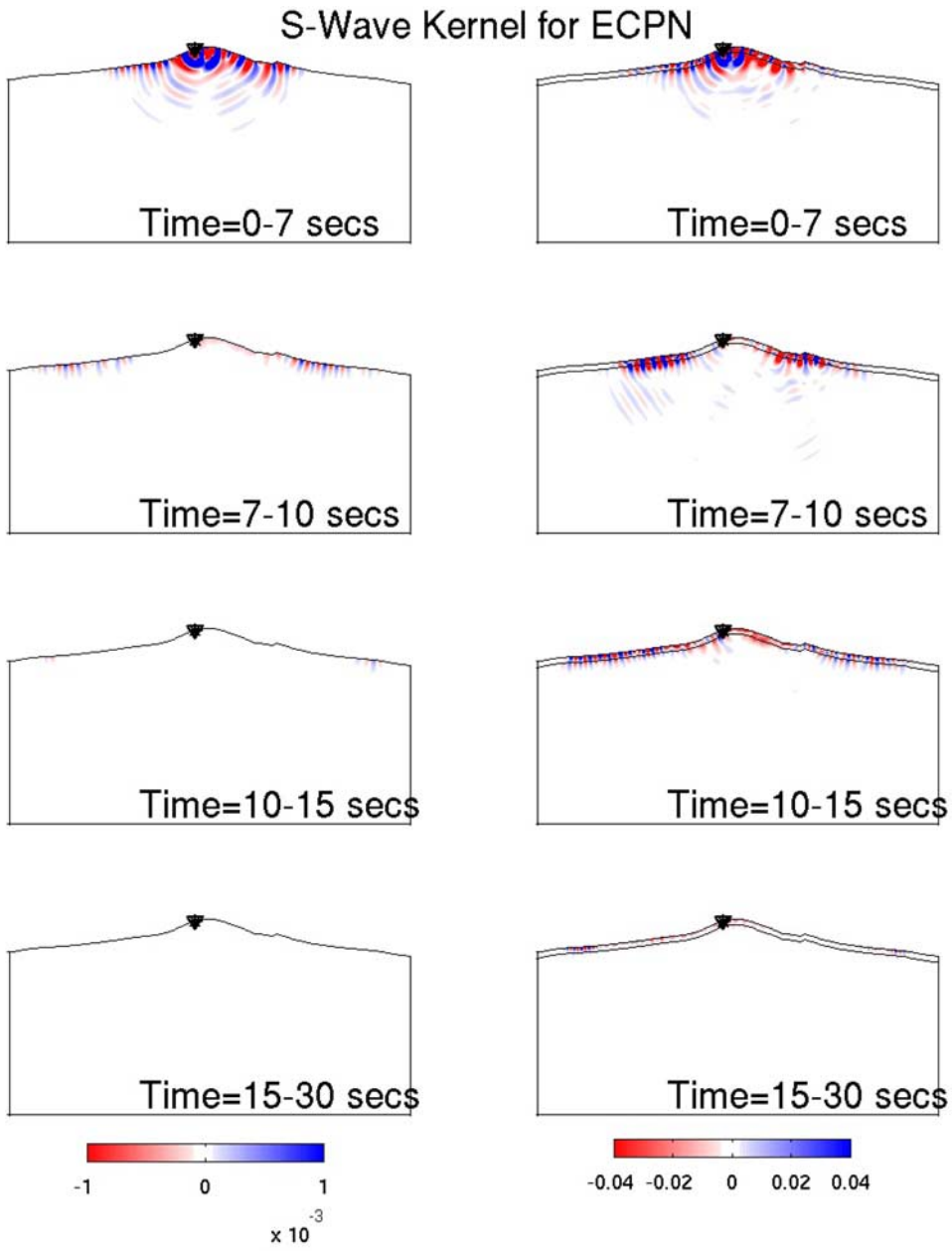

Figure 15. *S* wave sensitivity kernels for station ECPN, for the (left) homogeneous and (right) layered models. See Figure 13.

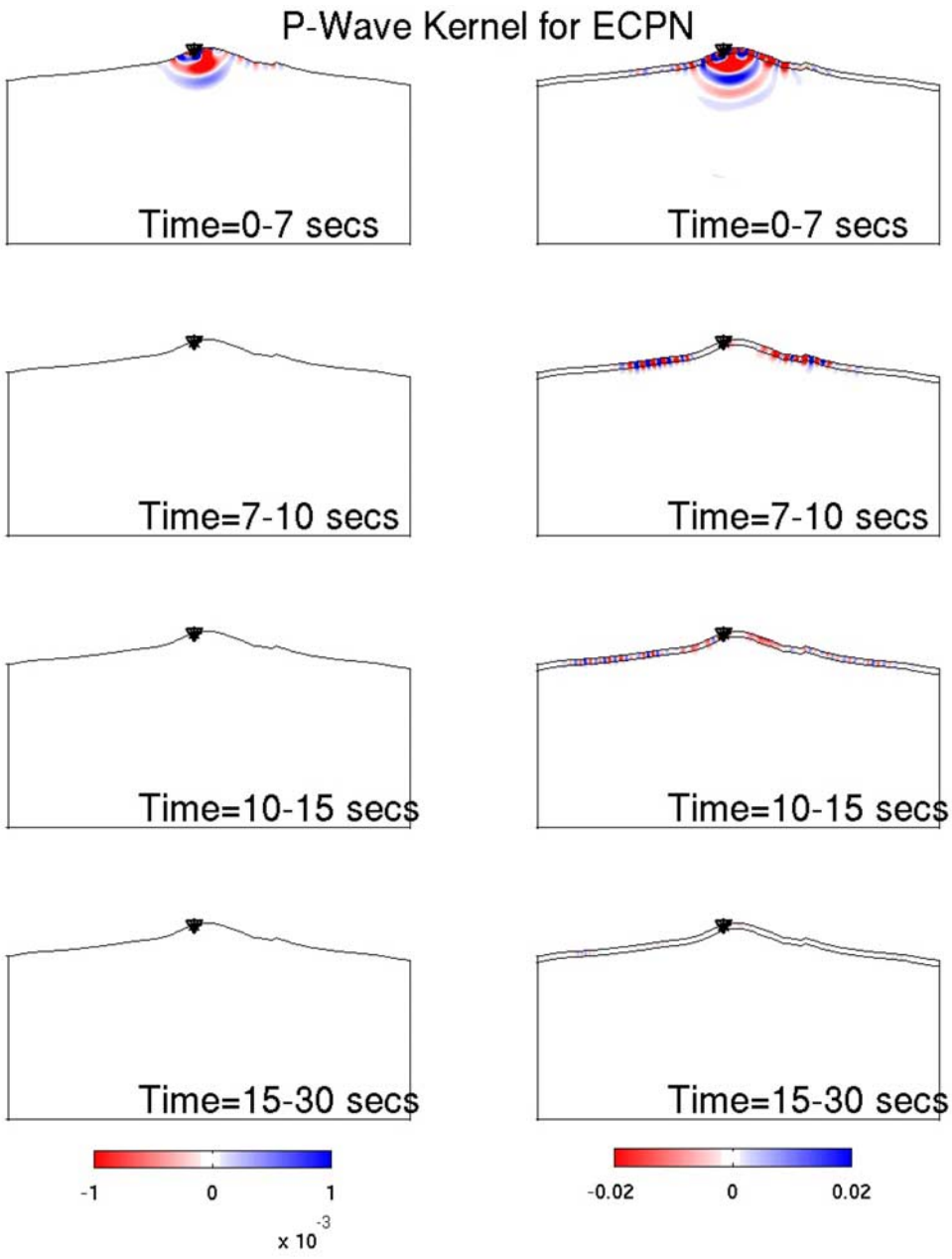

Figure 16. *P* wave sensitivity kernels for station ECPN, for the (left) homogeneous and (right) layered models. See Figure 13.

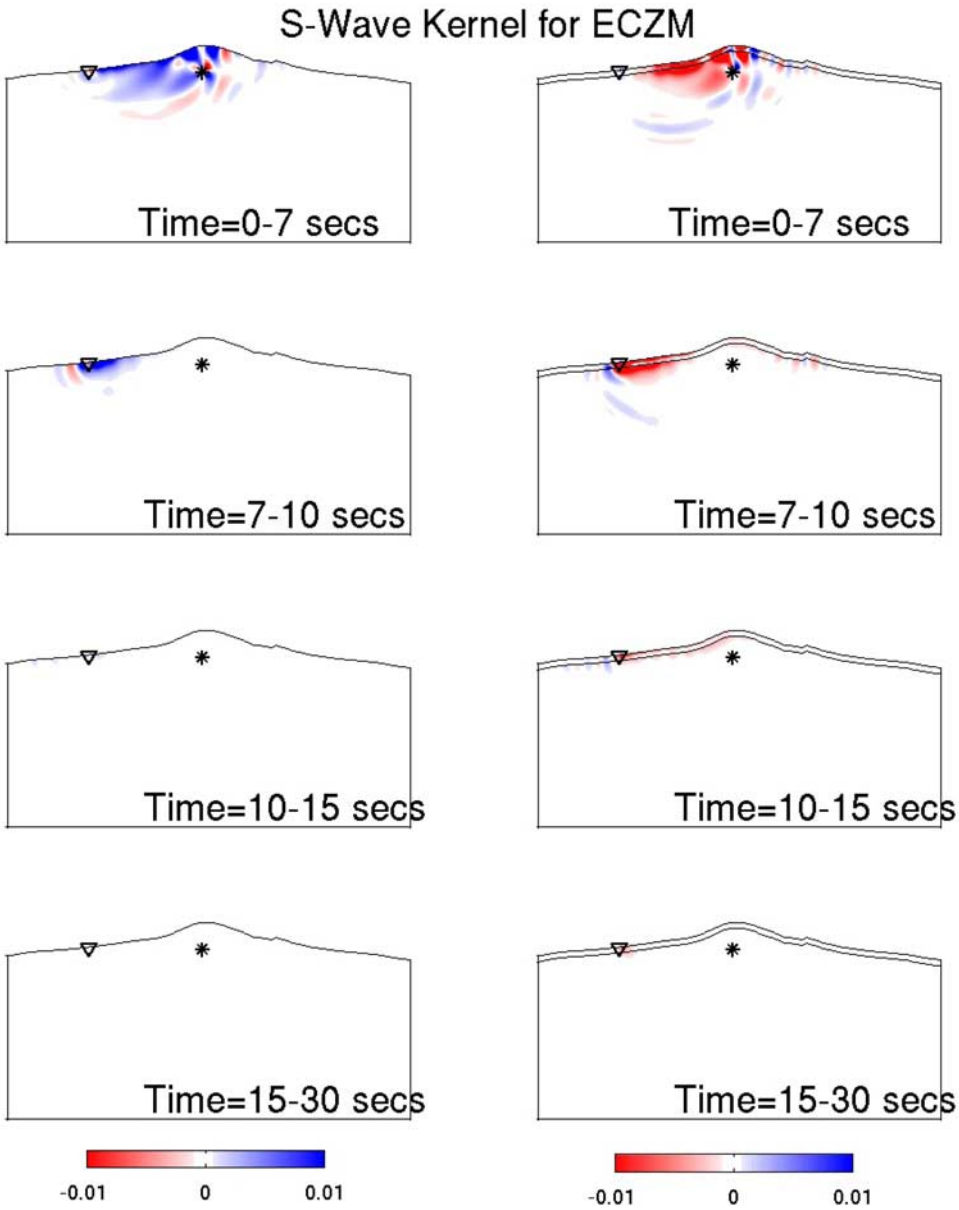

Figure 17. *S* wave sensitivity kernels for station ECZM, for the (left) homogeneous and (right) layered models. The rows represent the different seismogram time slices for which the kernels are calculated, as indicated. Units are Kg m^{-1} s^{-1}. Source (star) depth, 1800 m (1400 m below the base of the near surface low-velocity layer). Model is 20 km × 10 km.

[35] **Acknowledgments.** This work has been part supported by the EU FP6 projects SPICE-MRTN-CT-2003-504267 and VOLUME-018471 and the Irish Government's HEA-PRTLI COSMOGRID consortium. Simulations were run at the Irish Centre for High End Computing (ICHEC). Thanks to Gilberto Saccorotti and Jeroen Tromp for discussions and Edoardo Del Pezzo for comments on this paper.

References

Akaike, H. (1974), A new look at the statistical model identification, *IEEE Trans. Autom. Control*, *19*, 716–723, doi:10.1109/TAC.1974.1100705.

Almendros, J., B. Chouet, and P. Dawson (2001), Spatial extent of a hydrothermal system at Kilauea Volcano, Hawaii, *J. Geophys. Res.*, *106*, 13,565–13,580, doi:10.1029/2001JB000310.

Bruno, P., G. Cippitelli, and A. Rapola (1998), Seismic study of the Mesozoic carbonate basement around Mt. Somma-Vesuvius, Italy, *J. Volcanol. Geotherm. Res.*, *84*, 311–322, doi:10.1016/S0377-0273(98)00023-7.

Cesca, S., J. Battaglia, T. Dahm, E. Tessmer, S. Heimann, and P. Okubo (2008), Effects of topography and crustal heterogeneity on the source estimation of LP events at Kilauea volcano, *Geophys. J. Int.*, *172*, 1219–1236, doi:10.1111/j.1365-246X.2007.03695.x.

Chouet, B. (1986), Dynamics of a fluid-driven crack in three dimensions by the finite difference method, *J. Geophys. Res.*, *91*, 13,967–13,992, doi:10.1029/JB091iB14p13967.

Chouet, B. (1996), Long-period volcano seismicity: Its source and use in eruption forecasting, *Nature*, *380*, 309–316, doi:10.1038/380309a0.

Chouet, B., G. De Luca, G. Milana, P. Dawson, M. Martini, and R. Scarpa (1998), Shallow velocity structure of Stromboli Volcano, Italy, derived from small-aperture array measurements of Strombolian tremor, *Bull. Seismol. Soc. Am.*, *88*, 653–666.

Chouet, B., P. Dawson, T. Ohminato, M. Martini, G. Saccorotti, F. Giudicepietro, G. D. Luca, G. Milana, and R. Scarpa (2003), Source mechanisms of explosions at Stromboli Volcano, Italy, determined from moment tensor inversions of very-long period data, *J. Geophys. Res.*, *108*(B1), 2019, doi:10.1029/2002JB001919.

Corsaro, R. A., and M. Pompilio (2004), Buoyancy of magmas at Mt Etna, *Terra Nova*, *16*, 6–22.

Dawson, P., B. Chouet, P. G. Okubo, A. Villasenor, and H. M. Benz (1999), Three-dimensional velocity structure of the Kilauea caldera, Hawaii, *Geophys. Res. Lett.*, *26*, 2805–2808, doi:10.1029/1999GL005379.

De Luca, G., R. Scarpa, E. Del Pezzo, and M. Simini (1997), Shallow structure of Mt. Vesuvius volcano, Italy, from seismic array analysis, *Geophys. Res. Lett.*, *24*, 481–484, doi:10.1029/97GL00169.

Ferrazzini, V., K. Aki, and B. Chouet (1991), Characteristics of seismic waves composing Hawaiian volcanic tremor and gas-piston events observed by a near-source array, *J. Geophys. Res.*, *96*, 6199–6209, doi:10.1029/90JB02781.

Fink, A. (1997), Time reversed acoustics, *Phys. Today*, *50*, 34–40, doi:10.1063/1.881692.

Harrington, R. M., and E. E. Brodsky (2007), Volcanic hybrid earthquakes that are brittle-failure events, *Geophys. Res. Lett.*, *34*, L06308, doi:10.1029/2006GL028714.

Julian, B. R. (1994), Volcanic tremor: Nonlinear excitation by fluid flow, *J. Geophys. Res.*, *99*, 11,859–11,877, doi:10.1029/93JB03129.

Kumagai, H., and B. Chouet (1999), The complex frequencies of long-period seismic events as probes of fluid composition beneath volcanoes, *Geophys. J. Int.*, *138*, F7–F12, doi:10.1046/j.1365-246X.1999.00911.x.

Kumagai, H., B. Chouet, and M. Nakano (2002a), Waveform inversion of oscillatory signatures in long-period events beneath volcanoes, *J. Geophys. Res.*, *107*(B11), 2301, doi:10.1029/2001JB001704.

Kumagai, H., B. A. Chouet, and M. Nakano (2002b), Temporal evolution of a hydrothermal system in Kusasutsu-Shirane Volcano, Japan, inferred from the complex frequencies of long-period events, *J. Geophys. Res.*, *107*(B10), 2236, doi:10.1029/2001JB000653.

Kumagai, H., B. Chouet, and P. Dawson (2005), Source process of long-period event at Kilauea volcano, Hawaii, *Geophys. J. Int.*, *161*, 243–254, doi:10.1111/j.1365-246X.2005.02502.x.

Legrand, D., S. Kaneshima, and H. Kawakatsu (2000), Moment tensor analysis of near-field broadband waveforms observed at Aso Volcano, Japan, *J. Volcanol. Geotherm. Res.*, *101*, 155–169, doi:10.1016/S0377-0273(00)00167-0.

Lokmer, I., G. Saccorotti, B. Di Lieto, and C. J. Bean (2008), Temporal evolution of long-period seismicity at Etna Volcano, Italy, and its relationships with the 2004–2005 eruption, *Earth Planet. Sci. Lett.*, *266*, 205–220, doi:10.1016/j.epsl.2007.11.017.

Menke, W. (1984), *Geophysical Data Analysis: Discrete Inverse Theory*, 260 pp., Elsevier, Orlando, Fla.

Métaxian, J.-P., P. Lesage, and J. Dorel (1997), Permanent tremor at Masaya Volcano, Nicaragua: Wave field analysis and source location, *J. Geophys. Res.*, *102*, 22,529–22,545, doi:10.1029/97JB01141.

Mora, M., P. Lesage, B. Valette, G. E. Alvarado, C. Leandro, J.-P. Métaxian, and J. Dorel (2006), Shallow velocity structure and seismic site effects at Arenal volcano, Costa Rica, *J. Volcanol. Geotherm. Res.*, *152*, 121–139, doi:10.1016/j.jvolgeores.2005.09.013.

Nakano, M., and H. Kumagai (2005), Waveform inversion of volcano-seismic signals assuming possible source geometries, *Geophys. Res. Lett.*, *32*, L12302, doi:10.1029/2005GL022666.

Nakano, M., H. Kumagai, and B. A. Chouet (2003), Source mechanism of long-period events at Kusatsu-Shirane Volcano, Japan, inferred from waveform inversion of the effective excitation functions, *J. Volcanol. Geotherm. Res.*, *122*, 149–164, doi:10.1016/S0377-0273(02)00499-7.

Nakano, M., H. Kumagai, B. Chouet, and P. Dawson (2007), Waveform inversion of volcano-seismic signals for an extended source, *J. Geophys. Res.*, *112*, B02306, doi:10.1029/2006JB004490.

Neuberg, J., and T. Pointer (2000), Effects of volcano topography on seismic broadband waveforms, *Geophys. J. Int.*, *143*, 239–248, doi:10.1046/j.1365-246x.2000.00251.x.

Neuberg, J., R. Luckett, B. Baptie, and K. Olsen (2000), Models of tremor and low frequency earthquake swarms on Monserrat, *J. Volcanol. Geotherm. Res.*, *101*, 83–104, doi:10.1016/S0377-0273(00)00169-4.

Neuberg, J., H. Tuffen, L. Collier, D. Green, T. Powell, and D. Dingwell (2006), The trigger mechanism of low-frequency earthquakes on Montserrat, *J. Volcanol. Geotherm. Res.*, *153*, 37–50, doi:10.1016/j.jvolgeores.2005.08.008.

O'Brien, G. S., and C. J. Bean (2004a), A 3D discrete numerical elastic lattice method for seismic wave propagation in heterogeneous media with topography, *Geophys. Res. Lett.*, *31*, L14608, doi:10.1029/2004GL020069.

O'Brien, G. S., and C. J. Bean (2004b), A discrete numerical method for modeling volcanic earthquake source mechanisms, *J. Geophys. Res.*, *109*, B09301, doi:10.1029/2004JB003023.

Ohminato, T., and B. Chouet (1997), A free surface boundary condition for including 3D topography in finite-difference method, *Bull. Seismol. Soc. Am.*, *87*, 494–515.

Ohminato, T., B. A. Chouet, P. Dawson, and S. Kedar (1998), Waveform inversion of very long period impulsive signals associated with magmatic injection beneath Kilauea Volcano, Hawaii, *J. Geophys. Res.*, *103*, 23,839–23,862, doi:10.1029/98JB01122.

Patanè, D., G. Barberi, O. Cocina, P. De Gori, and C. Chiarabba (2006), Time-resolved seismic tomography detects magma intrusions at Mount Etna, *Science*, *313*, 821–823, doi:10.1126/science.1127724.

Ripperger, J., H. Igel, and J. Wasserman (2003), Seismic wave simulation in the presence of real volcano topography, *J. Volcanol. Geotherm. Res.*, *128*, 31–44, doi:10.1016/S0377-0273(03)00245-2.

Saccorotti, G., B. Chouet, and P. Dawson (2003), Shallow-velocity models at the Kilauea Volcano, Hawaii, determined from array analyses of tremor wavefields, *Geophys. J. Int.*, *152*, 633–648, doi:10.1046/j.1365-246X.2003.01867.x.

Saccorotti, G., L. Zuccarello, E. Del Pezzo, J. Ibanez, and S. Gresta (2004), Quantitative analysis of the tremor wavefield at Etna Volcano, *J. Volcanol. Geotherm. Res.*, *136*, 223–245, doi:10.1016/j.jvolgeores.2004.04.003.

Saccorotti, G., I. Lokmer, C. J. Bean, G. Di Grazia, and D. Patane (2007), Analysis of sustained long-period activity at Etna Volcano, Italy, *J. Volcanol. Geotherm. Res.*, *160*, 340–354, doi:10.1016/j.jvolgeores.2006.10.008.

Talagrand, O., and P. Courtier (1987), Variational assimulation of meterological observations with a joint vorticity equation I: Theory, *Q. J. R. Meteorol. Soc.*, *113*, 1311–1328, doi:10.1256/smsqj.47811.

Tarantola, A. (1984), Inversion of seismic reflection data in the acoustic approximation, *Geophysics*, *49*, 1259–1266, doi:10.1190/1.1441754.

Tarantola, A. (1987), Inversion of travel times and seismic waveforms, in *Seismic Tomography*, edited by G. Nolet, pp. 135–157, Springer, Dordrecht, Netherlands.

Tarantola, A. (1988), Theoretical background for the inversion of seismic waveforms, including elasticity and attenuation, *Pure Appl. Geophys.*, *128*, 365–399, doi:10.1007/BF01772605.

Tarantola, A. (2006), Popper, Bayes and the inverse problem, *Nat. Phys.*, *2*, 492–494, doi:10.1038/nphys375.

Tromp, J., C. Tape, and Q. Liu (2005), Seismic tomography, adjoint methods, time reversal and banana-doughnut kernels, *Geophys. J. Int.*, *160*, 195–216, doi:10.1111/j.1365-246X.2004.02453.x.

Vasco, D. W. (1989), Deriving source-time functions using principal component analysis, *Bull. Seismol. Soc. Am.*, *79*, 711–730.

C. Bean, G. O'Brien, and I. Lokmer, Seismology and Computational Rock Physics Laboratory, School of Geological Sciences, University College Dublin, Belfield, Dublin 4, Ireland. (chris.bean@ucd.ie)